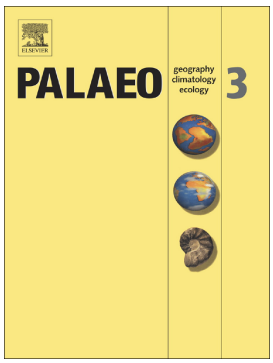

Convergent continental margin volcanic source for ash beds at the Permian-Triassic boundary, South China: Constraints from trace elements and Hf-isotopes

Xiangdong Wang, Peter A. Cawood, Laishi Zhao, Zhong-Qiang Chen, Zhengyi Lyu, Biao Ma

PII: S0031-0182(17)31076-3
DOI: doi:10.1016/j.palaeo.2018.02.011
Reference: PALAEO 8669

To appear in: *Palaeogeography, Palaeoclimatology, Palaeoecology*

Received date: 22 October 2017
Revised date: 9 February 2018
Accepted date: 9 February 2018

Please cite this article as: Xiangdong Wang, Peter A. Cawood, Laishi Zhao, Zhong-Qiang Chen, Zhengyi Lyu, Biao Ma , Convergent continental margin volcanic source for ash beds at the Permian-Triassic boundary, South China: Constraints from trace elements and Hf-isotopes. The address for the corresponding author was captured as affiliation for all authors. Please check if appropriate. Palaeo(2017), doi:10.1016/j.palaeo.2018.02.011

Convergent continental margin volcanic source for ash beds at the Permian−Triassic boundary, South China: Constraints from trace elements and Hf-isotopes

Xiangdong Wang[1], Peter A. Cawood[2, 3], Laishi Zhao[1, *], Zhong-Qiang Chen[4, *], Zhengyi Lyu[1], Biao Ma[1]

[1] State Key Laboratory of Geological Processes and Mineral Resources, China University of Geosciences (Wuhan), Wuhan 430074, China.

[2] Department of Earth, Atmosphere and Environment, Monash University, Victoria 3800, Australia

[3] Department of Earth Sciences, University of St Andrews, KY16 9AL, UK

[4] State Key Laboratory of Biogeology and Environmental Geology, China University of Geosciences (Wuhan), Wuhan 430074, China

*Corresponding authors: Laishi Zhao (zlscug@163.com); Zhong-Qiang Chen (zhong.qiang.chen@cug.edu.cn)

Abstract

Volcanic activity around the time of the Permian−Triassic boundary (PTB) has been proposed as a trigger for the associated biocrisis. Multiple claystone beds are prominent near the PTB sections in South China. Twenty one PTB ash beds from three sections at Shangsi, Jianshi and Meishan in South China were sampled and analyzed. Volcanic ash geochemistry indicate dacite and rhyolite compositions. Zircons from the ash layers yield comparatively low Nb/Hf and high Th/Nb ratios, falling in the range of arc/orogenic-related settings. Zircon Hf-isotope compositions show that $\varepsilon_{Hf}(t)$ values vary from −11.7 to 1.8, indicating involvement of both juvenile and ancient crustal components. The ash beds (SS27a, JS129, JS130, JS133，MS25, MS26) near the biotic extinction horizon display a large variation in ε_{Hf} (t) and relatively positive average values, indicating input of juvenile mantle or crust, and implying rapid transit through the older basement of the South China Craton. Spatial

and temporal distribution of ash beds from thirty one PTB sections worldwide reveal that volcanic ash beds occur mainly in, or proximal to, the Tethys region and were sourced locally. Integration of Hf-isotope and trace-element compositions from magmatic zircons suggests that the PTB volcanism occurred along the convergent continent margin in, or near, southwestern South China as a result of the closure of the Paleo-Tethys Ocean.

1. Introduction

The Permian–Triassic (252 million years ago) mass extinction (PTME) constitutes the greatest biocrisis experienced by life on Earth since the evolution of multicellular organisms some 600 million years ago. The cause of this catastrophic event has remained enigmatic with a number of kill mechanisms being proposed, including extreme climate warming (Sun et al., 2012; Chen et al., 2016), ocean acidification (Payne et al., 2010; Clarkson et al., 2015), ocean anoxic event (Wignall and Twitchett, 1996; Shen et al., 2010; Algeo et al., 2011), acid rain (Algeo et al., 2011; Black et al., 2012, 2014), and toxic metal poisoning (Sanei et al., 2012; Grasby et al., 2017). Increasing evidence shows that the volatile release from the Siberian Traps Large Igneous Province (STLIP) is likely the primary trigger of these kill mechanisms, and drove the end-Permian mass extinction (Wignall, 2001; Svensen et al., 2009; Algeo et al., 2011; Sobolev et al., 2011; Black et al., 2012, 2014; Burgess and Bowring, 2015. Burgess et al., 2017). Volcanic ash is common in Upper Permian and Lower Triassic strata throughout South China (Yin et al., 1992). Some ash layers are associated with biotic extinction horizons (e.g., Bed 25 of Meishan section) and this volcanism has been invoked as part of the trigger mechanism for the PTME (Gao et al., 2013; He et al., 2014). In this paper, we establish the source of these ash beds and their link with the PTME.

Volcanic ash layers from across the Permian–Triassic boundary in South China were analyzed at the Shangsi, Jianshi and Meishan sections. The PTME within these regions has been calibrated to an interval within the *Clarkina meishanensis* and *Isarcicella staeschei* conodont zones (Chen et al., 2015). All three sections contain

abundant ash layers, now altered to clay, which lie below, within and above the P–T boundary. We collected 9 clay layers from the Shangsi section, 6 from the Jianshi section, and 6 from the Meishan section to analyze their petrology, whole-rock geochemistry and zircon U-Pb ages, trace elements, and Hf-isotope compositions. These data enable an assessment of volcanic source (STLIP vs Paleo-Tethyan subduction), and their frequency distribution with respect to the PTME.

2. Geologic settings and sampling

2.1. Shangsi section

The Shangsi section is located near Changjianggou village of Shangsi Town, Guangyuan City, Sichuan Province. The Shangsi area lies on the northwestern margin of the South China Craton (Fig. 1B). The Permian–Triassic succession is continuously exposed and is well studied (Mundil et al., 2004; Riccardi et al., 2007; Shen et al., 2011; Chen et al., 2016). The upper Changhsingian (latest Permian) succession is composed of alternating thin-bedded cherty limestone and siliceous mudstone of the Dalong Formation. The lowest Triassic (Griesbachian) strata consist of interbeds of marlstone and mudstone of the Feixianguan Formation. Volcanic ash claystones are present through the succession. Nine ash layers (SS-23-4.2, SS-23-1.6, SS-23, SS-25, SS-27a, SS-27c, SS-28a, SS-29c-d, and SS-33) are recognized and sampled. Individual ash beds range from 2 cm to 26 cm in thickness, and span from the *Clarkina changxingensis-yini* conodont zone to the *Isarcicella isarcica* zone (Jiang et al., 2011).

2.2 Jianshi section

This section, near Jianshi county, southwest Hubei province, is located on the north margin of the South China Craton (Fig. 1B). The succession through the late Permian and the P–T boundary is well exposed and six volcanic clay layers are identified and were sampled (JS103, JS128, JS129, JS130, JS133, JS135). Few studies have been undertaken on this section and are limited to biostratigraphy (Mao et al., 2013; Lyu et al., 2017). The Late Permian succession at the Jianshi section is

termed the Dalong Formation and consists of carbonaceous mudstone, mudstone, siliceous limestone, and interbedded clay layers. It is overlain by the early Griesbachian Daye Formation composed of calcareous mudstone and argillaceous limestone with volcanic ash interbeds (Ma, 2012; Mao et al., 2013). Sampled ash layers are about 2 cm thick, expect bed JS103, which has a thickness of approximately 25 cm. The ash beds extend from the *C. changxingensis-yini* Zone to *H. parvus* Zone (Lyu et al., 2017).

2.3 Meishan section

The Meishan section is located at Meishan Town in Changxing County, Zhejiang Province and was situated at the northeastern margin of the South China Craton (Fig. 1B). This section is the Global Stratotype for the Permian–Triassic boundary (Yin et al., 2001). Biostratigraphy, lithofacies, geochronology, and geochemistry of the Meishan section have been extensively investigated since the 1980's (Burgess et al., 2014; Chen et al., 2015, and references therein). The uppermost Permian succession (Beds 20-24) comprises bioclastic limestone of the Changxing Formation, whereas the lowest Triassic strata consist of calcareous mudstone and marlstone of the Yinkeng Formation (Chen et al., 2015). Six ash beds between 4-10 cm thick are conspicuous in the field, and were labeled as MS-25, MS-26, MS-32, MS-37, MS-48, and MS-48+1.3. Of these, Bed 25 and Bed 26 lie within the *C. meishanensis* and *H. changxingensis* conodont zones, respectively. The remaining ash beds are within the *I. isarcica* conodont zone.

3. Methods

3.1. Samples preparation

Samples were divided into two parts; one for whole-rock analysis and another for zircon analysis. Zircon separation followed standard techniques involving crushing, heavy liquid, and magnetic separation techniques, followed by hand-picking of zircons under a binocular microscope and mounting in epoxy resin prior to polishing. Before analysis, zircon grains were photographed in transmitted and reflected light,

then imaged by cathodoluminescence (CL) to document size, external morphology, internal structure and inclusions, in order to choose spots for U–Pb age, trace element, and Hf isotope analyses.

3.2. Mineralogical and whole-rock compositions

The mineral composition of the ashes were determined by X-ray diffraction at the State Key Laboratory of Geological Processes and Mineral Resources China University of Geosciences (Wuhan (SKLGPMR of CUG)), China. Whole-rock major element analysis was performed via dissolution by Atomic Fluorescence Spectrometer at CUG. A pre-ignition was used to determine the loss on ignition. Uncertainty was generally less than 5 %. Trace elements were analyzed at SKLGPMR of CUG with ICP–MS (Agilent 7500a). The Blank and national standards AGV-2, BHVO-2, BCR-2, RGM-2 were selected for calibrating element concentration. The detailed sample dissolution procedure, the analytical process, and accuracy of analyses are outlined by Liu et al (2008).

3.3. Zircon U–Pb dating and trace-element analysis

Zircon U-Pb ages and trace elements were analyzed at SKLGPMR. Detailed analytical procedures and data processing follow Liu et al. (2010). An Agilent 7500a ICP-MS was employed to acquire ion-signal intensity. The carrier gas was helium. Nitrogen was added to the central gas flow (Ar+He) of the Ar plasma to decrease the detection limit, improve precision and increase the sensitivity for most elements by a factors of 2-3 (Hu et al., 2012). Harvard zircon 91500 was used as an external standard for U-Pb dating to correct for both instrumental mass bias and isotopic fractionation, and was analyzed twice every 5 unknowns. Trace element concentrations were calculated according to multiple-reference material calibration combined with internal standardization (Liu et al., 2010). Zircon standard GJ-1 was the control standard and was analyzed twice every ~15 analyses. Uncertainties of individual analysis were reported as 1σ. Selection of analytical signals, time-drift correction, and quantitative calibration were determined using ICPMSDataCal

software (Liu et al., 2010). Primitive mantle and chondrite standardize values are from Sun and McDonough (1989).

3.4. Hf isotopic analysis

Hf isotopic analyses were conducted using the Neptune (Plus) MC-ICPMS system with an excimer laser at SKLGPMR. Analyses were performed using a spot size of 44 um with helium acting carrier gas. Testing was performed using the model of single point erosion with a laser repetition rate of 10 Hz at 100 mJ/pulse. The detail instrumental parameters and experimental conditions are the same as those Hu et al. (2012). Standard 91500 was used as external standard with two analyses following every 8 unknowns. Zircon standards GJ-1 and TEM were analyzed as unknown and were conducted before and after sample analysis. The mass fractionation of Yb was used to correct the mass fractionation of Lu because of the similar physiochemical properties (Liu et al., 2010). The values of 0.7938 for $^{176}Yb/^{173}Yb$ and 0.02656 for $^{176}Lu/^{175}Lu$ are used for interference correction of ^{176}Lu and ^{176}Yb to ^{176}Hf, respectively (Blichert-Toft and Albarede, 1997). Time-dependent drift of Lu-Hf isotopic ratios were corrected using a linear interpolation (with time) according to the variations of standard 91500. The chondritic values of $^{176}Hf/^{177}Hf = 0.282772$ and $^{176}Lu/^{177}Hf = 0.0332$ were chosen for the calculation of $\varepsilon_{Hf}(t)$ values (Blichert-Toft and Albarede, 1997). $^{176}Lu/^{177}Hf$ ratios of zircon were used for calculating the one-stage model ages (T_{DM1}), according to the hypothesis the depleted mantle reservoir possesses a linear Hf isotopic growth from $^{176}Hf/^{177}Hf = 0.279718$ at 4.55 Ga to 0.283250 at present (Griffin et al., 2000). Two stage model ages (T_{DM2}) were calculated under the assumption that protolith of the zircon sourced from depleted mantle and had the composition of the average continental crust with $^{176}Lu/^{177}Hf$ of 0.0150 (Griffin et al., 2002). The selection of analytical signal and quantitative calibration were operated with ICPMSDataCal software (Liu et al., 2010).

4. Results

4.1. Mineral compositions

Analysis by XRD reveal the samples consist of mixed-layer of illite and smectite (21 % to 92 %), plagioclase (2 % to 61 %), quartz (1 % to 44 %), chlorite (0 % to 20 %), and gypsum (0 % to 48 %) with minor pyrite, alkali feldspar and calcite (Table S1). Previous analyses by Gao et al. (2013) and He et al. (2014) found similar mineral compositions for the tuff layers. The high content of clay minerals suggests that the samples have experienced intensive alteration, presumably after primary volcanic glass.

4.2. Whole rock Major and trace elements

Major and trace element data for the samples from the three sections are listed in Table S.3. The analysis have large loss-on-ignitions (8.0 wt. % ≤ LOI ≤ 16.4 wt. %，except for SS28), which is consistent with their high clay content. The samples have very similar REE and trace element spider patterns (Fig. 2). They are moderately to highly enriched in light rare earth elements (LREEs) ($(Sm/La)_N$ = 0.2 to 1.0). The fractionation of heavy rare earth elements (HREEs) is low ($(Gd/Yb)_N$ at about 1.0). All samples have strong negative Eu anomalies with Eu/Eu* = 0.2 to 0.7 (Table S2). Trace element spider plots are characterized by negative Nb, Sr, Ta and Ti anomalies and positive Th, U and Pb anomalies (Fig. 2), and are similar to subduction-related rocks (Pearce et al., 1995).

4.3. Zircon morphology

Most zircon grains are euhedral, translucent, and prismatic, sometimes with a light grey color. The grains are commonly 80-160 μm in length but some in SS23-1.6 exceed 200 μm. They are dominated by columnar shapes with aspect ratios ranging from 2.0 to approximately 4.0. Nearly all the grains have a core-rim structure, the rims always show well-developed oscillatory zoning. Cores have either oscillatory zoning or gray-colorless homogeneous internal structure (Fig. 3A, B, C). Oscillatory zoning and prismatic shape indicate that they are of magmatic origin. In general, zircons from different horizons display a range of internal structure and external morphology, whereas the zircons from one sample and the same horizon show similar

morphology. There appear to be very few inherited zircons and they tend to be stubby prismatic or granular. They often have unclear oscillatory zoning with inhomogeneous structure (e.g. JS129-6, JS133-12 and MS37-1). The details can be found in Fig. 3.

4.4. Zircon U-Pb ages

We selected 749 zircon grains for U-Pb analysis, of which, 332 grains are from nine ash beds at the Shangsi section, 210 grains from six ash beds at the Jianshi section, and 207 grains from six beds at the Meishan section (Table S3, Fig. 4). In each section, the ages can be divided into three groups. The first group includes ages less than 240 Ma, which are younger than the age of the main peak and the established depositional age of the beds. They are interpreted to be grains that have suffered Pb loss and they constitute less than 2% of analyzed grains. The second group occupy ~95 % of all analyzed grains, have ages ranging from 240 Ma to 270 Ma (Table S3), and were used for calculating the mean age of each ash bed. The last group, are ages older than 270 Ma, and range from 273 Ma to 2473 Ma. The grains are interpreted as inherited or xenocrystic zircons that crystallize prior to eruption of the volcanic source (Mundil et al., 2001).

The dominant grains (Group 2) that are inferred to be contemporaneous with volcanic eruption, and hence date the time of eruption. They are long prismatic grains with clear oscillatory zoning or homogeneous internal structure. Inherited zircon in most cases are stubby prismatic or granular, with unclear oscillatory zoning or inhomogeneous internal structure. Group 1 grains show no distinctive features to enable their recognition.

Individual mean ages of 21 tuff horizons from the three sections vary from ~251.5 Ma to ~256.7 Ma, and fall largely in the range 252-253 Ma (Table 4, 7). Because all ages of each section overlap within errors, mean age of all the tuff beds from each of the three sections was calculated and displayed in Fig. 4. The mean ages (Fig. 4) are equivalent to the established age of the Permian–Triassic boundary (~252 Ma) (Burgess et al., 2014). In combination with the conodont biostratigraphic data, the U-Pb zircon ages indicate that the source of the ash horizons was from volcanic

eruptions contemporaneous with the time of sediment accumulation near PTB.

4.5. Zircon trace elements

The overall chondrite-normalized REE patterns of zircons in each sample are characterized by HREE enrichment relative to the LREE and MREE with positive Ce and negative Eu anomalies; features typical of unaltered magmatic zircons (Hoskin, 2003; El-Bialy and Ali, 2013). The mean of positive Ce anomalies range from 2.1 to 12.1 and negative Eu anomalies are mostly ≤ 0.25 (Table S7). The markedly negative Eu anomalies imply a major role of feldspar fractionation prior to (or during) zircon crystallization (El-Bialy and Ali, 2013). The analyzed zircon grains show a large variation in total REE abundances, varying from 401 to 11532 ppm (Table. S7). The chondrite-normalized values of LREE from the analyzed zircons vary from 1 to 10 (Fig. 5), which is the normal range of igneous zircons (Hoskin, 2003). In addition, MREE display slight enrichment, and HREE fluctuate within the typical range of 10^3 or 10^4 of chondrite (Fig. 5).

Y contents of the analyzed zircons vary from 414 to 16756 ppm, but are mostly in the range 414-5989 ppm (Table S5, 7). Hf contents in the analyzed samples range from 6860 to 39340 ppm with most greater than 9000 ppm (Table S5, 7), which is a feature of evolved felsic magma (Claiborneet al., 2010). Zircons from all the analyzed samples contain Th and U ranging from 22-2963 ppm and 38-2992 ppm, respectively. Th/U values are 0.15-2.2, but most are more than 0.5 (Table S5, 7), which is a feature of igneous zircons (El-Bialy and Ali, 2013; Hoskin, 2003). The abundance of Nb and Ta in all the zircons fall within the range of unaltered magmatic zircon (Nb ≤ 8 ppm, Ta ≤ 3 ppm; El-Bialy and Ali, 2013).

The chondrite-normalized REE patterns of zircon grains from volcanic ashes in South China are difference from those associated with rocks of the STLIP. Zircons from STLIP rocks display steeper chondrite-normalized REE patterns, Ce anomalies are more significant, and Eu anomalies are less obvious (Fig. 5).

In general, Nb content of magmatic arc magmas is relatively depleted to that of the within-plate settings, and arc zircons possess lower Nb/Hf and higher Th/Nb.

These ratios are capable of assessing tectonic setting through the effects of continental contamination and crystallization of Th-rich minerals (Yang et al., 2012). The zircons from the analyzed ash beds mostly fall within the orogenic (arc-related) field on the basis of Th/Nb, Hf/Th, Nb/Hf, Th/U ratios (Fig. 8; Yang et al., 2012). Trace element data for the analyzed zircons are listed in Table S5.

4.6. Zircon Hf isotope composition

Hf isotope analyses were undertaken on 336 magmatic zircons from the 21 samples from the three sections. The majority of the analyses (332) had U-Pb ages corresponding with the PTME with the remaining analyses from inherited grains. The grains with PMTE ages display a wide range of Hf isotope compositions, with ε_{Hf} (t) values varying from -11.7 to 1.8 (Table S6, 7, Fig. 7C). The one-stage model ages (T_{DM1}) and the two-stage model ages (T_{DM2}) vary from 1361 Ma to 850 Ma and 2015 Ma to 1169 Ma, respectively. Zircons from beds near the extinction horizon, such as SS27a, JS129, MS25, DXK9a-b display overall more positive averages (Table S6, 7, Fig. 9) relative to beds above or below the extinction horizon. Similar Hf isotope compositions of ash beds were also observed at the Daxiakou section by Gao et al. (2013) (Fig. 9). Analyses for four inherited zircons show relatively negative ε_{Hf}(t) values of -17.7, -15.5, -11.0, and -8.3, corresponding to U-Pb ages of 1004 Ma, 702 Ma, 509 Ma, and 401 Ma (Table S6, Fig. 7C). Their T_{DM2} ages are 2948 Ma, 2588 Ma, 2162 Ma, and 1911 Ma, which suggest that they were derived from reworked ancient crustal material.

5. Discussion

5.1. The global distribution of volcanic ash layers near the PTB

We have compiled 31 sections for the PTB from across the globe (Fig. 1A, B, Table S8). Results show that the PTB volcanic felsic ashes are widely spread across the Paleo-Tethys region. Volcanic ash beds or volcanic microfacies also occur near PTB in Iran (Abadeh, Shahreza, and Jofa sectiona) and Tibet (Wenbudangsang section), which in paleogeographic reconstructions are close to South China. But there

are no reports of ash horizons from other PTB sections, except for Sydney and Bowen basins, where multiple tuff horizons occur in middle Permian-early Triassic strata (Metcalfe et al., 2015) associated with subduction of the paleo-Pacific (Cawood, 2005; Cawood et al. 2011). In particular, there are no ash beds reported from areas more proximal to the Siberian traps in Canada, Greenland, and the Arctic (Fig. 1A, Table S8). This argues against the Siberian Traps as being the source for the ash. Of course, the presence or absence of volcanic ash beds depends in part on depositional topography, atmospheric circulation patterns, and hydrodynamic conditions. The Gujo-Hachiam section, Ubara section, and NF1212C section in Japan lack volcanic ash beds yet incorporate the PTB, perhaps reflecting distance from source and lying outside the principal dispersal direction of the ash. The North China Craton was emergent at this time and although terrestrial deposits occur, no ash horizons have been recognized. But the ChaHe and Zhejue sections in South China also accumulated in a terrestrial environment and 2 ash beds are recognized near the extinction horizon in these sections (Shen et al., 2011; He et al., 2014; Fang et al., 2017).

From the spatial distribution of ash horizons, southern South China is envisioned as the source region. Volcanic ash beds generally become more frequent and thicker towards southwestern margin of South China (He et al., 2014). Moreover, Xie et al., (2010) suggested that in South China the most intensive volcanism occurred in the southwest on the basis of increased evidence for cyanobacteria blooms in this direction.

5.2. The character of PTB volcanic ashes in South China

Our XRD data reveal that plagioclase and quartz are present in all the samples, suggesting derivation from silicic volcanic eruptions. The ash layers have negative Eu anomalies with Eu/Eu* of 0.18 to 0.73 and an average value of 0.45, which imply that the original source rocks crystallized calcium plagioclase. On the basis of Nb/Y versus Zr/TiO_2, the ashes are mainly dacitic to rhyolitic in composition (Fig. 6A). On the Al_2O_3 versus TiO_2 diagram (Fig. 6B), all the volcanic ashes fall into the compositional field of felsic rocks. The silicic composition of the ash beds further

argues against derivation from the mafic basalts of the Siberian Traps. Minor felsic rocks are reported from the Siberian traps but these have an age of 246.9 ± 2.6 Ma (Saraev et al., 2011), which is younger than the age of the ash beds in South China and of the PTB. More recently, Burgess and Bowing. (2015) and Burgess et al. (2017) showed mafic rocks dominated Siberian Traps across the PTB. The Triassic felsic rocks associated with the Siberian Traps are of very small volume relative to mafic rocks and are not associated with significant air fall units (Burgess and Bowing, 2015). This data argue against any significant felsic volcanism related to the Siberian Traps and thus make it unlikely that the traps were a source of the felsic tuffs in South China.

5.3. Source of the PTB volcanic ashes in South China

Multiple claystone beds are prominent near the PTB, mainly from *Clarkina yini* to *Isarcicella isarcica* conodont zones in South China. The majority of the magmatic zircons in these three sections have geochemical characteristics indicative of a continental crust affinity, including negative Eu anomalies (Fig. 2A), high Th and U abundances, and relatively high U/Yb (Fig. 7B) with varying but low Th/U (0.15-2.2, Table S5, S7; Fig. 5). In contrast, zircons derived directly from a mantle source including the Siberian traps lack prominent Eu anomalies (Fig. 5), with low Th and U contents and exceptional high Th/U (Fig. 7A) (Hoskin, 2003; Siebel et al., 2009; Liu et al., 2014). The three sections in South China have similar Hf-isotope composition, suggesting that the magmas are from a similar source. Zircon Hf-isotope compositions show that $\varepsilon_{Hf}(t)$ values vary from -11.7 to 1.8 (Fig. 7C), indicating that at least two components have been involved: juvenile lower crust/mantle and ancient middle-upper crust. The Siberian Traps are mainly composed of mafic basalts with zircon $\varepsilon_{Hf}(t)$ of 2.3-15.5 (Fig. 7c) (Malitch et al., 2010), indicative of a mainly mantle source. Subduction related magmatism within the Ailaoshan suture zone, along the southern margin of the South China Craton, has yielded U–Pb ages of 251.6 Ma-247.5 Ma and $\varepsilon_{Hf}(t)$ ranging from −3.1 to −11.1(Fig. 7C) (Liu et al., 2015), similar to the PTB volcanic ashes.

Hf-isotope compositions of correlative ash layers in the three sampled sections are similar (Fig. 9), indicating derivation of individual layers from the same source material. Whereas different layers from the same section, display variation in zircon Hf-isotope compositions (Fig. 9), implying a mixture of different proportions of the source material. The ash beds in *Clarkina yini* and *Isarcicella isarcica* conodont zones, away from the extinction interval, usually have Hf-isotope composition ranging from -11.7 to -2.0 (two-stage model ages: 2015 to 1402 Ma) (Fig. 9), indicating involvement of crust at least as old as Paleoproterozoic. However, the ash beds (SS27a, JS129, JS130, JS133, MS25, MS26) near the extinction horizon have ε_{Hf} (t) values as high as +1.8 (two-stage model age: 1169 Ma) (Fig. 9), implying that more juvenile lower crustal or mantle material had contributed to the volcanic activity.

5.4. Tectonic background of the PTB volcanic ashes in South China

In the late Permian and early Triassic, felsic magmatism was widespread around the margins of Pangea including the 18,000 km long Terra Australis orogen extending from northeastern Australia to northwestern South America (Gao et al., 2013, Cawood, 2005). In the Paleo-Tethys region, the Lhasa, Qiangtang, Baoshan, Sibumasu and Indochina blocks drift rapidly northwards ultimately assembling into Asia, resulting in extensive felsic magmatism associated with subduction of the Tethys Ocean and associated branch oceans (Zhu et al., 2009; Yang et al., 2011; Zi et al., 2012, 2013; Hu et al., 2014; Liu et al., 2015; Halpin et al., 2016). The whole rock geochemistry presented here shows that the volcanic ash horizons display enrichment in large ion lithophile elements and depletion in high field strength elements (Fig. 2B). Zircons from the ashes have Nb/Hf, Th/Nb and Hf/Th ratios similar to those from arc/orogenic-related settings (Fig. 8). Therefore, the PTB volcanism may have taken place along the convergent continent margin in, or near, southwestern South China as a result of the closure of the Paleo-Tethys Ocean. The most probable position is Song Ma-Ailaoshan-Jinshajiang suture zone based on the compatible timing and ε_{Hf} (t).

5.5. The relationship between felsic volcanism and P−T extinction

The Permian−Triassic boundary in South China is characterized by boundary clay layers. Growing evidence shows that volcanism near the Permian−Triassic boundary (PTB) may have contributed to the PTB biocrisis (Isozaki et al., 2007; Xie et al., 2010; Gao et al., 2013; Shen et al., 2012, 2013; He et al., 2014; Fang et al., 2017). The intensity and frequency of the volcanic activity appear to increase near the PTME interval. For example, three eruptions in Shangsi and Meishan, 5 eruptions in Daxiakou (Gao et al., 2013), and three or four eruptions in Jianshi section (Fig. 9), fall within 60 kyr of the PTME interval (Burgess et al., 2014). The ash layers in the South China sections relate to convergent continent margin activity and ash layers or volcanic microfacies occur across the Paleo-Tethys region, including the Wenbudangsang section, Lhasa terrane, and the Kuh-e-Hambas, Abadeh, Kuh-e-Ali-Bashi sections in Iran (Fig. 1A; Table S8). This indicates that not only was there frequent felsic igneous activity near the PTB but that it was also widespread.

Ash beds (SS27a, JS129, JS130, JS133, MS25, MS26) near biotic extinction horizon have relatively positive $\varepsilon_{Hf}(t)$ averages relative to the other layers (Fig. 9), perhaps implying involvement of more juvenile material contributed to the igneous activity. Pronounced negative shifts of $\delta^{13}C$ values were observed in volcanic ash layers (Shen et al., 2012), suggesting a direct relationship between igneous activity and the carbon cycle. Furthermore, felsic subduction-related volcanism is inherently more violent and explosive than mafic dominated LIP activity due to its higher volatile content, and thus more likely to result in input of gases and particles to the stratosphere resulting in their extensive distribution. Although the felsic volcanism is unlikely to have been a sole causative mechanism for the PTB biocrisis due to its small volume relatively to Siberian Traps, deposition of massive volcanic ashes does represent a hazard to local flora/fauna, including acidification, eutrophication and contamination of surface water that have been observed in modern eruptions (Sulpizio et al., 2014). Evidence of microbial proliferation is found directly from volcanic ashes during the Permian–Triassic transition (Fang et al., 2017), and enhancing bacterial colonization may also lead to environmental deterioration, such as decomposition of

organic matter and anoxia (Chen and Benton, 2012; Fang et al., 2017). Thus, the igneous activity associated with closure of the Paleo-Tethys may have further aggravated the environmental deterioration initiated by the Siberian Traps.

6. Conclusions

Three sections through the PTB in South China contain multiple volcanic ash beds. Major and trace element contents of the ashes, and zircon U-Pb, trace element and Hf isotope data indicate the following:

(1). Derivation from magmas of rhyolitic and dacitic compositions, and a subduction-related REE trace element pattern.

(2). Low Nb/Hf and high Th/Nb ratios of zircons, which lie within the range of arc/orogenic-related settings. The relatively high U/Yb values of zircons accord with a continental crust origin with a minor mantle component.

(3). Spatial and temporal distribution of ash beds from 31 PTB sections worldwide reveal that the PTB volcanic ashes occur largely in the Paleo-Tethys region, suggesting that volcanism is related to continental convergence associated with subduction of Tethyan oceanic lithosphere and assembly of Asia.

(4). Hf-isotope compositions show that ash beds near the biotic extinction horizon show relatively positive ε_{Hf} (t) averages, indicating increased input of juvenile mantle with limited interaction between magma and crust, implying rapid transit through the crust.

Acknowledgments

We are grateful to L. Zhang, Y. Li, D.R. Ma, P.A. Yan, F. Guo, C. Han and S.J. Liu for their assistance during the experimental studies. This study is supported by NSFC grants (41473006, 41272025, 41673011, 40972003, 41272023, 41572091). PAC acknowledges support from the Australian Research Council grant FL160100168.

This paper is a contribution to IGCP 630.

Figure captions

Fig. 1 Global paleogeography (A) (after (Algeo et al., 2013)), South China (B) (after (Algeo et al., 2013)), at the PTB (~252Ma). Numbering of sites conforms to Table S7. Abbreviations in A: Am = Amuria, In = Indonesia, Kz = Kazakhstan, NC = North China, Q = Qinling Ocean, SC = South China, Tm = Tarim. Abbreviations B: J = Jiangnan Uplift, K = Khamdian Uplift, N = Nanpanjiang Basin, Y–Z = Yunkai–Zhemin Uplifts. Paleogeography of world from http://jan.ucc.nau.edu/~rcb7/ Red and yellow stars represent the PTB sections yielding volcanic ash or microfacies beds, whereas the black and white stars indicate that these sections are barren of the PTB volcanic ash beds.

Fig. 2 Chondrite-normalized REE patterns (A) and Primitive mantle-normalized trace element patterns (B) of the PTB volcanic ashes in South China. REE concentrations of the subduction-related rocks and Siberian igneous rocks are from Liu et al. (2015) and Malitch et al. (2010), respectively. Chondrite and primitive mantle-normalizing values from McDonough (1989)

Fig. 3 Zircon cathodoluminescence (CL) images of volcanic ash beds from (A) Shangsi section, (B) Jianshi section and (C) Meishan section.

Fig. 4 Concordia and ages distribution diagrams of U–Pb isotope data for the zircons of volcanic ashes from Shangsi, Jianshi and Meishan sections.

Fig. 5 Chondrite-normalized REE patterns of zircons from the PTB volcanic ashes and Siberian igneous rocks. Zircon REE concentrations of Siberian igneous rocks are from Malitch et al. (2010).

Fig. 6 Discriminant diagrams of volcanic rock type using rock trace elements by whole rock geochemistry.

(A): Zr/TiO_2 versus Nb/Y diagram (Wilson, 1986), (B): TiO_2 versus Al_2O_3 diagram(He et al., 2014).

Fig. 7 Discriminant diagrams for zircon origin. (A): Th versus U (Liu et al., 2014), (B): U/Yb versus Y (Grimes et al., 2007); (C): Hf-isotope compositions of volcanic ash beds (from Shangsi section, Jianshi section, Meishan sections) in South China, the Siberian Traps (from Malitch et al (2010)), and granite at 251.6~ 247.5Ma from Ailaoshan structure zone (from Liu et al., 2015).

Fig. 8 Discriminant diagrams of tectonic settings for the volcanic ashes in South China. (A): Nb/Hf versus Th/U (Yang et al., 2012); (B): Hf/Th versus Th/Nb (Yang et al., 2012).

Fig. 9 Stratigraphic variations of the Hf-isotope compositions of magmatic zircons from ash beds of the Shangsi, Meishan, Jianshi and Daxiakou (Gao et al., 2013) sections. Conodont zones of the Shangsi, Meishan, Jianshi and Daxiakou sections follow Jiang et al. (2011), Chen et al. (2015), Lyu et al. (2017) and Zhao et al. (2013), respectively.

References

Algeo, T.J., Chen, Z.Q., Fraiser, M.L., Twitchett, R.J., 2011. Terrestrial–marine teleconnections in the collapse and rebuilding of Early Triassic marine ecosystems. Palaeogeogr. Palaeoclimatol. Palaeoecol. 308, 1-11.

Algeo, T.J., Henderson, C.M., Tong, J.N, Feng, Q.L., Yin, H.F., and Tyson, R.V., 2013. Plankton and productivity during the Permian–Triassic boundary crisis: An analysis of organic carbon fluxes. Glob. Planet. Chang.105, p. 52–67.

Black, B.A., Elkins-Tanton, L.T., Rowe, M.C., Peate, I.U., 2012. Magnitude and consequences of volatile release from the Siberian Traps. Earth Planet. Sci. Lett. 317–318, 363–373.

Black, B.A., Lamarque, A.F., Shields, C.A., Elkins-Tanton, L.T., Kiehl, J.T., 2014. Acid rain and ozone depletion from pulsed Siberian Traps magmatism. Geology 42, 67-70.

Blichert-Toft, J., and Albarede, F., 1997. The Lu-Hf isotope geochemistry of chondrites and the evolution of the mantle-crust system. Earth Planet. Sci. Lett. 148, 243–258.

Burgess, S.D., Bowring, S.A., and Shen, S.Z., 2014. High-precision timeline for Earth's most severe extinction. Proc. Natl. Acad. Sci. U. S. A. 111, 3316–3321.

Burgess, S.D., Bowring, S.A., 2015. High-precision geochronology confirms voluminous magmatism before, during, and after Earth's most severe extinction. Sci. Adv. 1, e1500470 (2015).

Burgess, S.D., Muirhead, J.D., Bowring, S.A., 2017. Initial pulse of the Siberian Traps sills as the trigger of the end-Permian mass extinction. Nat. Commun. 18, 164.

Cawood, P.A., 2005. Terra Australis Orogen: Rodinia breakup and development of the Pacific and Iapetus margins of Gondwana during the Neoproterozoic and Paleozoic. Earth-Sci. Rev. 69, 249–279.

Cawood, P.A., Leitch, E.C., Merle, R.E., Nemchin, A.A., 2011. Orogenesis without collision: Stabilizing the Terra Australis accretionary orogen, eastern Australia.

Geol. Soc. Am. Bull. 123, 2240-2255.

Chen, Z.Q., Benton,M.J., 2012. The timing and pattern of biotic recovery following the end Permian mass extinction. Nat. Geosci. 5, 375–383.

Chen, Z.Q., Yang, H., Luo, M., Benton, M.J., Kaiho, K., Zhao, L.S., Huang, Y.G., Zhang, K.X., Fang, Y.H., Jiang, H.S., Qiu, H., Li, Y., Tu, C.Y., Shi, L., Zhang, L., Feng, X.Q., and Chen, L., 2015. Complete biotic and sedimentary records of the Permian–Triassic transition from Meishan section, South China: Ecologically assessing mass extinction and its aftermath. Earth-Sci. Rev. 149, 67–107.

Chen, J., Shen S.Z., Li, X.H., Joachimski, M.M., Bowring, S.A., Erwin, D.H., Yuan, D.X., Chen, B., Zhang, H., Wang, Y., Cao, C.Q., Zheng, Q.F., Mu, L., 2016. High-resolution SIMS oxygen isotope analysis on conodont apatite from South China and implications for the end-Permian mass extinction. Palaeogeogr. Palaeoclimatol. Palaeoecol. 448, 26–38.

Clarkson, M.O., Kasemann, S.A., Wood, R.A., Lenton, T.M., Daines, S.J., Richoz, S., Ohnemueller, F., Meixner, A., Poulton, S.W., Tipper, E.T., 2015. Ocean acidification and the Permo-Triassic mass extinction. Science 348, 229-232.

Claiborne, L.L., Miller, C.F., and Wooden, J.L., 2010. Trace element composition of igneous zircon: a thermal and compositional record of the accumulation and evolution of a large silicic batholith, Spirit Mountain, Nevada. Contrib. Mineral. Petrol. 160, 511–531.

Dobretsov, N.L., Kirdyashkin, A.A., Kirdyashkin, A.G., Vernikovsky, V.A., Gladkov, I.N., 2008. Modelling of thermochemical plumes and implications for the origin of the Siberian traps. Lithos 100, 66–92.

El-Bialy, M.Z., and Ali, K.A., 2013. Zircon trace element geochemical constraints on the evolution of the Ediacaran (600–614 Ma) post-collisional Dokhan Volcanics and Younger Granites of SE Sinai, NE Arabian–Nubian Shield. Chem. Geol. 360–361, 54–73.

Fang, Q., Hong, H.L., Chen, Z.Q., Yu, J.X., Wang, C.W., Yin, K., Zhao, L.L., Liu, Z., Cheng, F., Gong, N.N., Furnes, H., 2017. Microbial proliferation coinciding with volcanism during the Permian–Triassic transition: New, direct evidence from

volcanic ashes, South China. Palaeogeogr. Palaeoclimatol. Palaeoecol. 474, 164–186.

Gao, Q.L., Zhang, N., Xia, W.C., Feng, Q.L., Chen, Z.Q., Zheng, J.P., Griffin, W.L., O'Reilly, S.Y., Pearson, N.J., Wang, G.Q., Wu, S., Zhong, W.L., and Sun, X.F., 2013. Origin of volcanic ash beds across the Permian–Triassic boundary, Daxiakou, South China: Petrology and U–Pb age, trace elements and Hf-isotope composition of zircon. Chem. Geol. 360–361, 41–53.

Griffin, W.L., Pearson, N.J., Belousova, E., Jackson, S.E., van Achterbergh, E., O'Reilly, S.Y., and Shee, S.R., 2000. The Hf isotope composition of cratonic mantle: LAM-MC-ICPMS analysis of zircon megacrysts in kimberlites. Geochim. Cosmochim. Acta. 64, 133–147.

Griffin, W.L., Wang, X., Jackson, S.E., Pearson, N.J., O'Reilly, S.Y., Xu, X.S., and Zhou, X.M., 2002. Zircon chemistry and magma mixing, SE China: in-situ analysis of Hf isotopes, Tonglu and Pingtan igneous complexes. Lithos 61, 237–269.

Grimes, C.B., John, B.E., Kelemen, P.B., Mazdab, F.K., Wooden, J.L., Cheadle, M.J., Hanghøj, K., Schwartz, J.J., 2007. Trace element chemistry of zircons from oceanic crust: A method for distinguishing detrital zircon provenance. Geology 35, 643–646.

Grasby, S.E., Shen, W.J., Yin, R.S., Gleason, G.D., Blum, J.D., Lepak, R.F., Hurley, J.P., Beauchamp, B., 2017. Isotopic signatures of mercury contamination in latest Permian Oceans. Geology 45, 55–58.

Halpin, J.A., Tran, H.T., Lai, C.K., Meffre, S., Crawford, A.J., and Zaw, K., 2016. U–Pb zircon geochronology and geochemistry from NE Vietnam: A ‘tectonically disputed’ territory between the Indochina and South China blocks. Gondwana Res. 34, 254–273.

He, B., Zhong, Y.T., Xu, Y.G., and Li, X.H., 2014. Triggers of Permo–Triassic boundary mass extinction in South China: The Siberian Traps or Paleo-Tethys ignimbrite flare-up? Lithos 204, 258–267.

Hoskin, P.W.O., 2003. The composition of zircon and igneous and metamorphic

petrogenesis. Rev. Minera. Geochem. 53, 27–62.

Hu, P.Y., Li, J., Wang, M., Xie, C.M., Wu, YW., 2014. Zircon U–Pb–Hf isotopes and whole-rock geochemistry of gneissic granites from the Jitang complex in Leiwuqi area, eastern Tibet, China: Record of the closure of the Paleo-Tethys Ocean. Tectonophysics 623, 83–99.

Hu, Z.C., Liu, Y.S., Gao, S., Xiao, S.Q., Zhao, L.S., Günther, D., Li, M., Zhang, W., and Zong K.Q., 2012. A "wire" signal smoothing device for laser ablation inductively coupled plasma mass spectrometry analysis. Spectrochimica Acta Part B 78, 50–57.

Hu, P.Y., Li, C., Li, J., Wang, M., Xie, C.M., and Wu, Y.W., 2014. Zircon U–Pb–Hf isotopes and whole-rock geochemistry of gneissic granites from the Jitang complex in Leiwuqi area, eastern Tibet, China: Record of the closure of the Paleo-Tethys Ocean. Tectonophysics 623, 83–99.

Isozaki, Y., Shimizu, N., Yao, J.X., Ji, Z.S., and Matsuda, T., 2007. End-Permian extinction and volcanism-induced environmental stress: The Permian–Triassic boundary interval of lower-slope facies at Chaotian, South China. Palaeogeogr. Palaeoclimatol. Palaeoecol. 252, 218–238.

Isozaki, Y, 2009. Integrated ‘‘plume winter" scenario for the double-phased extinction during the Paleozoic–Mesozoic transition: The G-LB and P–TB events from a Panthalassan perspective. J. Asian Earth Sci. 36, 459-480.

Jiang, H.S., Lai, X.L., Yan, C.B., Aldridge, R.J., Wignall, P.B., and Sun, Y.D., 2011. Revised conodont zonation and conodont evolution across the Permian–Triassic boundary at the Shangsi section, Guangyuan, Sichuan, South China. Glob. Planet. Chang. 77, 103–115.

Liu, D., Zhao, Z.D., Zhu, D.C., Niu, Y.L., and Mark, H.T., 2014. Zircon xenocrysts in Tibetan ultrapotassic magmas: Imaging the deep crust through time. Geology 42, 43–46.

Liu, H.C., Wang, Y.J., Cawood, P.A., Fan, W.M., Cai, Y.F., and Xing, X.W., 2015. Record of Tethyan ocean closure and Indosinian collision along the Ailaoshan suture zone (SW China). Gondwana Res. 27, 1292–1306

Liu, Y.S., Hu, Z.C., Gao, S., Gunther, D., Xu, J., Gao, C.G., and Chen, H.H., 2008. In situ analysis of major and trace elements of anhydrous minerals by LA-ICP-MS without applying an internal standard. Chem. Geol. 257, 34–43.

Liu, Y.S., Gao, S., Hu, Z.C., Gao, C.G., Zong, K.Q., and Wang, D.B., 2010. Oceanic Crust Recycling-induced Melt-Peridotite Interactions in the Trans-North China Orogen: U-Pb Dating, Hf Isotopes and Trace Elements in Zircons from Mantle. J. Petrology 51, 537–571.

Lyu, Z.Y., Orchard, M.J., Chen, Z.Q., Wang, X.D., Zhao, L.S., Han, C., 2017. Uppermost Permian to Lower Triassic conodont successions from the Enshi area, western Hubei Province, South China. Palaeogeogr. Palaeoclimatol. Palaeoecol., in press, http://dx.doi.org/10.1016/j.palaeo.2017.08.015.

Mao, Y., Ma, Q., Feng, Q., 2013. Discovery of fish microremains in the Gufeng formation at the Luojiaba section from Jianshi, west Hubei (Chinese with English abstract). Acta Micropalaeontologica Sinica 30, 175-183.

Malitch, K.N., Belousova, E.A., Griffin, W.L., Badanina, I.Y., and Pearson, N.J., 2010. Magmatic evolution of the ultramafic-mafic Kharaelakh intrusion (Siberian Craton, Russia): insights from trace-element, U-Pb and Hf-isotope data on zircon. Contrib. Mineral. Petrol. 159, 753–768.

Metcalfe, I., Crowley, J.L., Nicoll, R.S., Schmitz, M., 2015. High-precision U-Pb CA-TIMS calibration of middle Permian to Lower Triassic sequences, mass extinction and extreme climate-change in eastern Australian Gondwana. Gondwana Res. 28, 61-81.

Mundil, R., Metcalfe, I., Ludwig, K.R., Renne, P.R., Oberil, F., and Nicoll, R., 2001. Timing of the Permian–Triassic biotic crisis: implications from new zircon U/Pb age data (and their limitations). Earth Planet. Sci. Lett. 187, 131–145.

Mundil, R., Ludwing, K.R., Metcalfe, I., and Renne, P.B., 2004. Age and timing of the Permian mass extinctions: U/Pb dating of closed-system zircons. Science 305, 1760–1763.

Payne, J.L., Turchyn, A.V., Paytan, A., DePaolo, D.J., Lehrmann, D.J., Yu, M.Y., Wei, J.Y., 2010. Calcium isotope constraints on the end-Permian mass extinctions.

Proc. Natl. Acad. Sci. U. S. A. 107, 8543-8548.

Pearce, J.A., Baker, P.E., Harvey, P.K., and Luff, I.W., 1995. Geochemical evidence for subduction fluxes, mantle melting and fractional crystallization beneath the South Sandwich island arc. J. Petrol. 36, 1073–1109.

Reichow, M.K., Pringle, M.S., Al'Mukhamedov, A.I., Allen, M.B., Andreichev, V.L., Buslov, M.M., Davies, C.E., Fedoseev, G.S., Fitton, J.G., Inger, S., Medvedev, A.Y., Mitchell, C., Puchkov, V.N., Safonova, I.Y., Scott, I.A., and Saunders, A.D., 2009. The timing and extent of the eruption of the Siberian Traps large igneous province: Implications for the end-Permian environmental crisis. Earth Planet. Sci. Lett. 277, 9–20.

Riccardi, A., L Kump, R., Arthur, M.A., and D'Hondt, S., 2007. Carbon isotopic evidence for chemocline upward excursions during the end-Permian event. Palaeogeogr. Palaeoclimatol. Palaeoecol. 248, 73–81.

Shen, Y.N., Farquhar, J., Zhang, H., Masterson, A., Zhang, T.G., Wing, B.A., 2010. Multiple S-isotopic evidence for episodic shoaling of anoxic water during Late Permian mass extinction. Nat. Geosci. 2, 210.

Shen, S.Z., Crowley, J.L., Wang, Y., Bowring, S.A., Erwin, D.H., Sadler, P.M., Cao, C.Q., Rothman, D.H., Henderson, C.M., Ramezani, J., Zhang, H., Shen, Y.N., Wang, X.D., Wang, W., Wu, L., Li, W.Z., Tang, Y.G., Liu, X.L., Liu, L.J., Zeng, Y., and Jin, Y.G., 2011. Calibrating the end-Permian mass extinction. Science 334, 1367–1372.

Shen, J., Algeo, T.J., Hu, Q., Zhang, N., Zhou, L., Xia, W.C., Xie, S.C., Feng, Q.L., 2012. Negative C-isotope excursions at the Permian–Triassic boundary linked to volcanism. Geology 40, 963-966.

Siebel, W., Schmitt, A.K., Danišík, M., Chen, F.K., Meier, S., and Weiß, S., 2009. Prolonged mantle residence of zircon xenocrysts from the western Eger rift. Nat. Geosci. 2, 886–890.

Sobolev, S.V., Sobolev, A.V., Kuzmin, D.V., Krivolutskaya, N.A., Petrunin, A.G., Arndt, N.T., Radko, V.A., Vasiliev, Y.R., 2011. Linking mantle plumes, large igneous provinces and environmental catastrophes. Nature 477, 312-316.

Sanei, H., Grasby, S.E., Beauchamp, B., 2012. Latest Permian mercury anomalies. Geology 40, 63–66.

Sun, S.S., and McDonough, W.F., 1989. Chemical and isotopic systematics of oceanic basalts: implications for mantle composition and processes. Geolog. Soc. London Spe. Pub. 42, 313–345.

Sun, Y.D., Joachimski, M.M., Wignall, P.B., Yan, C.B., Chen, Y.L., Jiang, H.S., Wang, L.N., Lai, X.L., 2012. Lethally Hot Temperatures during the Early Triassic Greenhouse. Science 338, 366-370.

Sulpizio, R., Zanchetta, G., Caron, B., Dellino, P., Mele, D., Giaccio, B., Insinga, D., Paterne, M., Siani, G., Costa, A., Macedonio, G., Santacroce, R., 2014. Bull. Volcan. 76, 866.

Svensen, H., Planke, S., Polozov, A.G., Schmidbauer, N., Corfu, F., Podladchikov, Y.Y., Jamtveit, B., 2009. Siberian gas venting and the end-Permian environmental crisis. Earth Planet. Sci. Lett. 277, 490–500.

Tohver, E., Lana, C., Cawood, P.A., Fletcher, I.R., Jourdan. F., Sherlock, S., Rasmussen, B., Trindade, R.I.F., Yokoyama, E., Souza Filho, C.R., Marangoni, Y., 2012. Geochronological constraints on the age of a Permo–Triassic impact event: U–Pb and $^{40}Ar/^{39}Ar$ results for the 40 km Araguainha structure of central Brazil. Geochim. Cosmochim. Acta. 86, 214–227.

Wilson, M., 1986,. A Chemical Classification of Volcanic Rocks Based on the Total Alkali-Silica Diagram. J. Petrol. 27, 745–750.

Wignall, P.B, Twitchett, R.J., 1996. Oceanic Anoxia and the End Permian Mass Extinction. Science 272, 1155-1158.

Wignall, P.B., 2001. Large igneous provinces and mass extinctions. Earth-Sci. Rev. 53, 1–33.

Xie, S.C., Pancost, R.D., Wang, Y.B., Yang, H., Wignall, P.B., Luo, G.M., Jia, C.L., and Chen, L., 2010. Cyanobacterial blooms tied to volcanisms during the 5.m.y. Permo–Triassic biotic crisis. Geology 38, 447–450.

Yang, J.H., Cawood, P.A., Du, Y.S., Huang, H., Huang, H.W., and Tao, P., 2012. Large Igneous Province and magmatic arc sourced Permian–Triassic

volcanogenic sediments in China. Sedim. Geol. 261–262, 120–131.

Yang, T.N., Zhang, H.R., Liu, Y.X., Wang, Z.L., Song, Y.C., Yang, Z.S., Tian, S.H., Xie, H.Q., and Hou, K.J., 2011. Permo–Triassic arc magmatism in central Tibet: Evidence from zircon U–Pb geochronology, Hf isotopes, rare earth elements, and bulk geochemistry. Chem. Geol. 284, 70–282.

Yin, H.F., et al., 1992. The effects of volcanism on the Permo–Triassic mass extinction in South China: In: Sweet, W.C., Yang, Z.Y., Dickons, M.D., and Yin, H.F., (Eds.), Permo–Triassic Events in the Eastern Tethys. Cambridge University Press, Cambrian, pp. 146–157.

Yin, H.F., Zhang, K.X., Tong, J.N. Yang, Z.Y., and Wu, S.B., 2001. The Global Stratotype Section and Point (GSSP) of the Permian–Triassic Boundary. China Basic Sci. 24, 102–114.

Zhao, LS, Chen, Y.L, Chen, Z.Q., and Cao, L., 2013. Uppermost Permian to Lower Triassic conodont zonation from three gorges area, South China. Palaios 28, 523–540.

Zhu, D.C., Mo, X.X., Niu, Y.L., Zhao, Z.D., Wang, L.Q., Pan, G.T., and Wu, F.Y., 2009. Zircon U–Pb dating and in-situ Hf isotopic analysis of Permian peraluminous granite in the Lhasa terrane, southern Tibet: Implications for Permian collisional orogeny and paleogeography. Tectonophysics 469, 48–60.

Zi, J.W., Cawood, P.A., Fan, W.M., Wang, Y.J., Tohver, E., McCuaig, T.C., and Peng, T.P., 2012. Triassic collision in the Paleo-Tethys Ocean constrained by volcanic activity in SW China. Litho, 144–145, 145–160

Zi, J.W., Cawood, P.A., Fan, W.M., Tohver, E., Wang, Y.J., Mccuaig, T.C., and Peng, T.P., 2013. Late Permian–Triassic magmatic evolution in the Jinshajiang orogenic belt, SW China and implications for orogenic processes following closure of the Paleo-Tethys. Am. J. of Sci. 313, 81–112.

Highlights

1. Volcanic ash beds covering the PTB in South China were derived from felsic magma emplaced into continental crust.

2. Volcanic ashes formed in a magmatic arc associated with subduction of Tethyan oceanic lithosphere and assembly of Asia.

3. Ash beds near the biotic extinction horizon display large variation in ε_{Hf} (t) and overall positive values, indicating increased input of juvenile mantle material at the PTB.

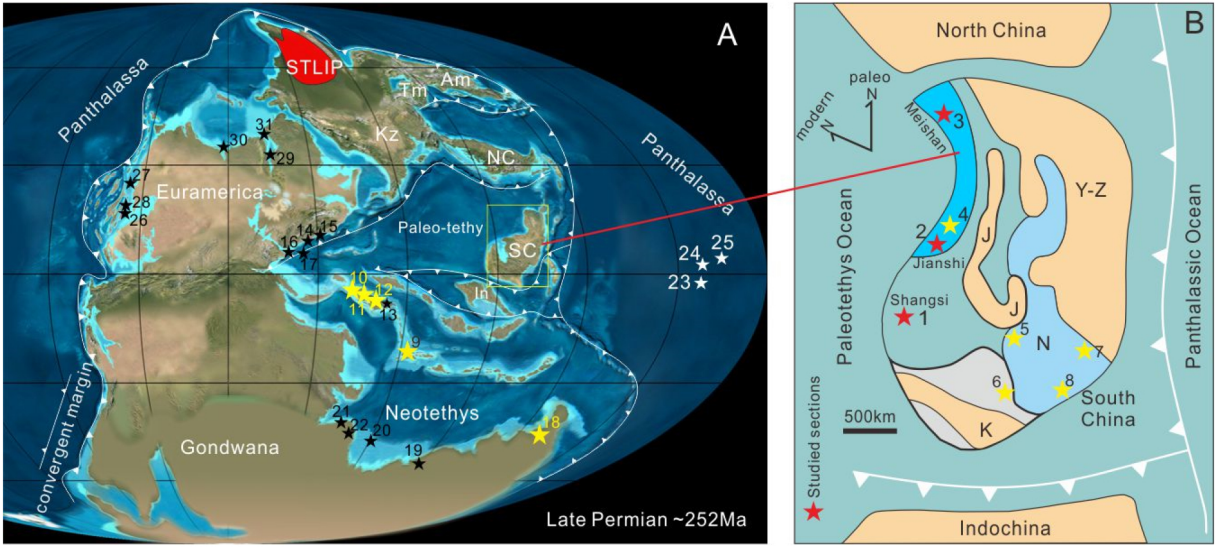
A
Panthalassa
STLIP
Tm
Am
Kz
NC
Euramerica
Paleo-tethy
SC
In
Panthalassa
convergent margin
Neotethys
Gondwana
Late Permian ~252Ma
B
North China
paleo N
modern N
Meishan
Y-Z
Jianshi
Shangsi
Paleotethys Ocean
Panthalassic Ocean
South China
500km
K
Studied sections
Indochina

Figure 1

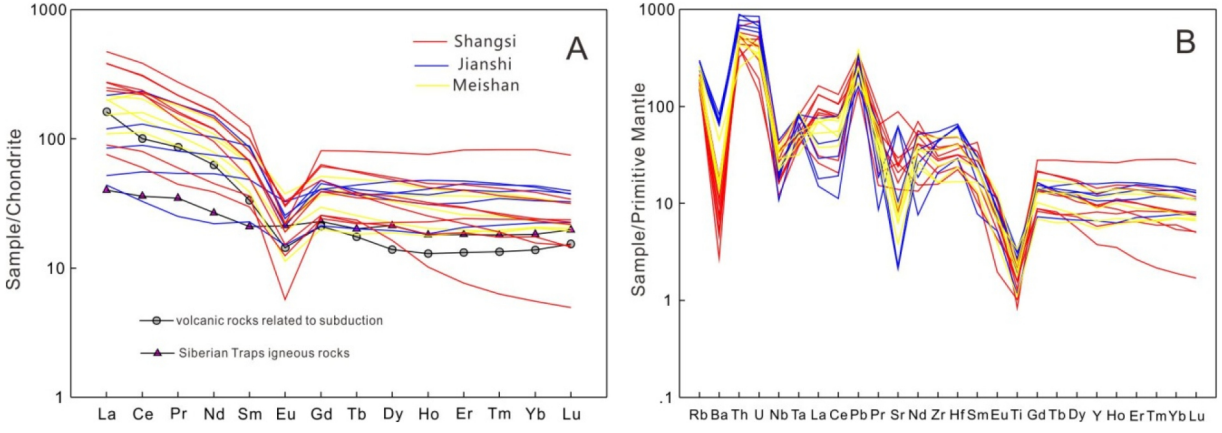
A
Shangsi
Jianshi
Meishan
Sample/Chondrite
1000
100
10
1
La Ce Pr Nd Sm Eu Gd Tb Dy Ho Er Tm Yb Lu
volcanic rocks related to subduction
Siberian Traps igneous rocks
B
Sample/Primitive Mantle
1000
100
10
1
.1
Rb Ba Th U Nb Ta La Ce Pb Pr Sr Nd Zr Hf Sm Eu Ti Gd Tb Dy Y Ho Er Tm Yb Lu

Figure 2

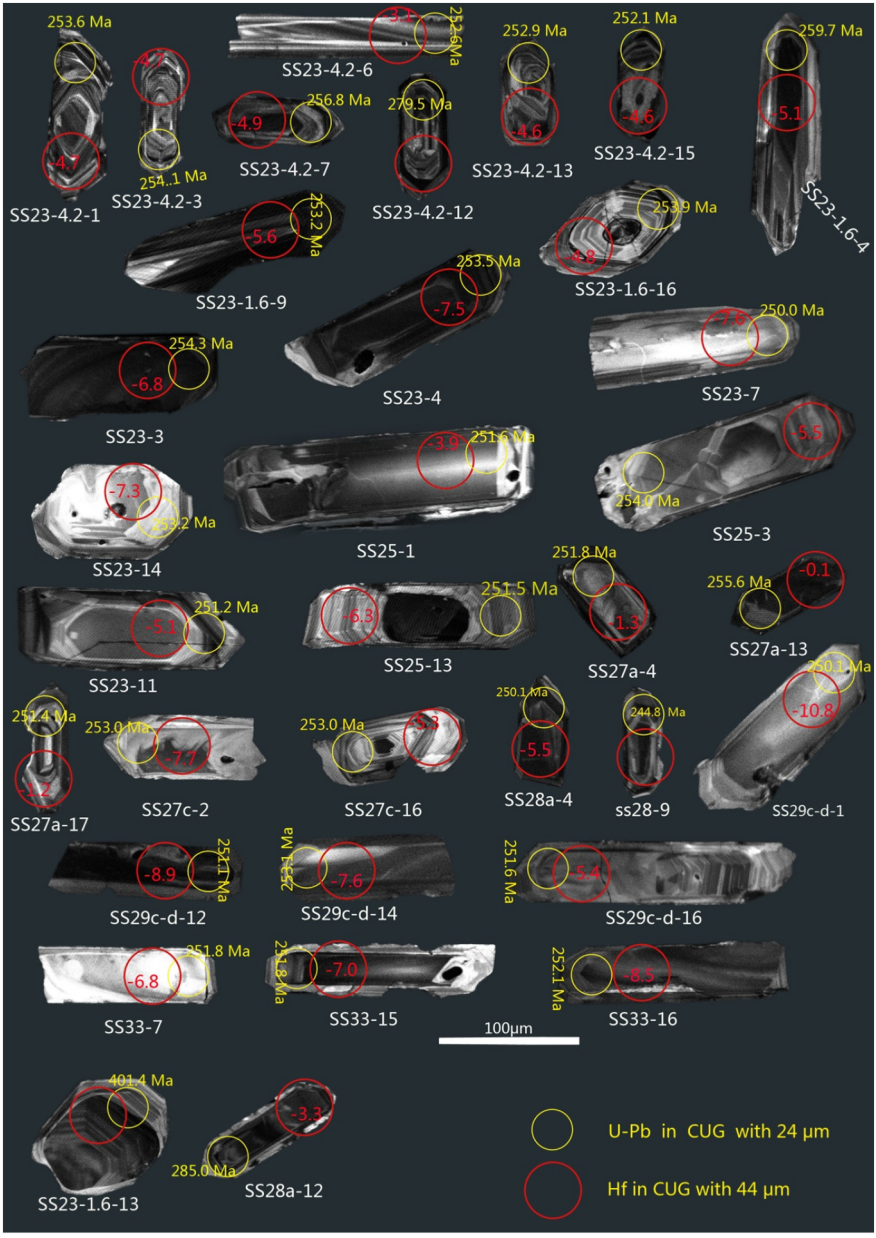
253.6 Ma
SS23-4.2-1
254.1 Ma
SS23-4.2-3
SS23-4.2-6
256.8 Ma
SS23-4.2-7
279.5 Ma
SS23-4.2-12
252.9 Ma
SS23-4.2-13
252.1 Ma
SS23-4.2-15
259.7 Ma
SS23-1.6-4
253.2 Ma
SS23-1.6-9
253.9 Ma
SS23-1.6-16
253.5 Ma
SS23-4
254.3 Ma
SS23-3
250.0 Ma
SS23-7
251.6 Ma
SS25-1
254.0 Ma
SS25-3
SS23-14
251.8 Ma
251.5 Ma
SS25-13
255.6 Ma
SS27a-13
251.2 Ma
SS23-11
SS27a-4
252.4 Ma
SS27a-17
253.0 Ma
SS27c-2
253.0 Ma
SS27c-16
250.1 Ma
SS28a-4
244.8 Ma
ss28-9
250.1 Ma
SS29c-d-1
251.1 Ma
SS29c-d-12
253.1 Ma
SS29c-d-14
251.6 Ma
SS29c-d-16
251.8 Ma
SS33-7
251.8 Ma
SS33-15
252.1 Ma
SS33-16
100μm
401.4 Ma
SS23-1.6-13
285.0 Ma
SS28a-12
U-Pb in CUG with 24 μm
Hf in CUG with 44 μm

A

Figure 3a

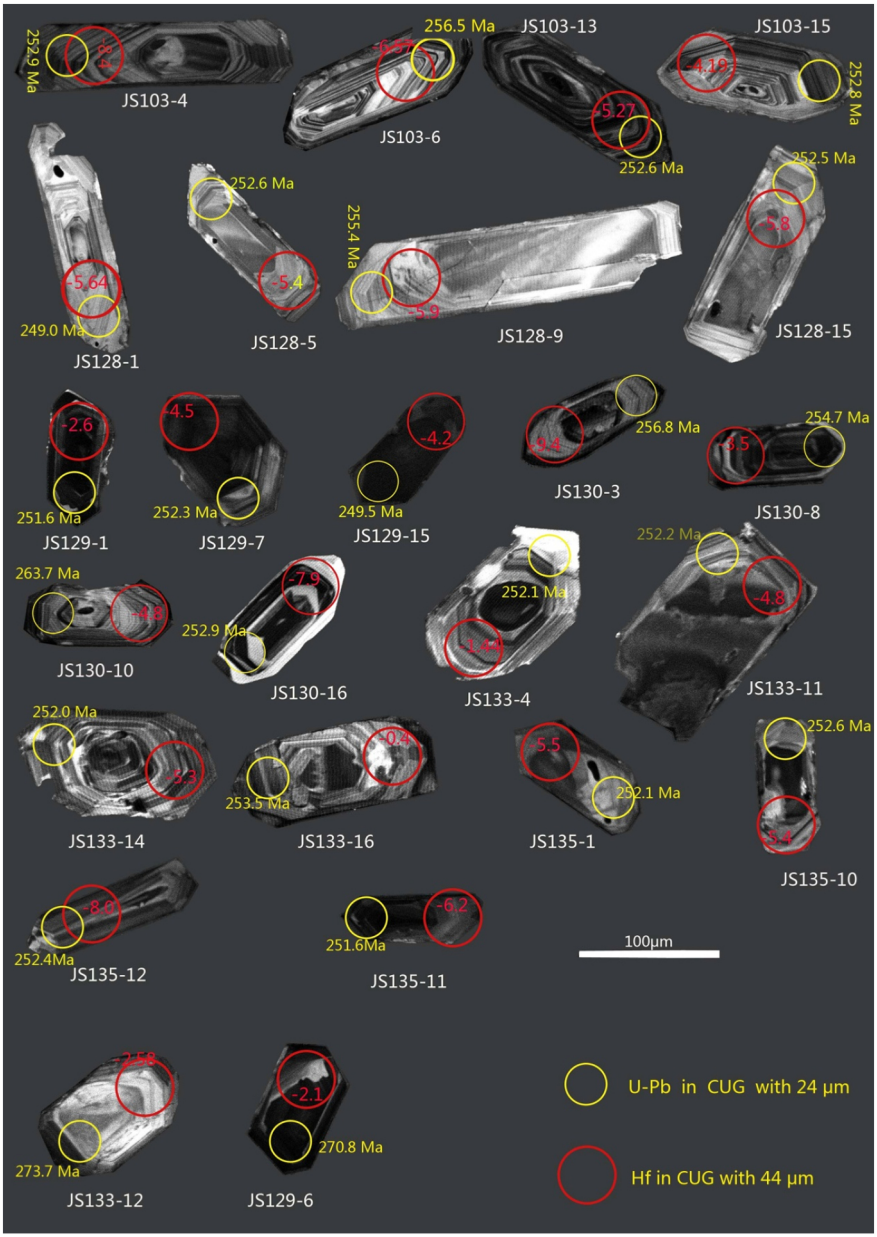
252.9 Ma
JS103-4
256.5 Ma
JS103-6
JS103-13
-5.27
252.6 Ma
JS103-15
-4.19
252.8 Ma
252.6 Ma
-5.4
255.4 Ma
JS128-9
252.5 Ma
-5.8
JS128-15
-5.64
249.0 Ma
JS128-1
JS128-5
-2.6
251.6 Ma
JS129-1
-4.5
252.3 Ma
JS129-7
-4.2
249.5 Ma
JS129-15
256.8 Ma
JS130-3
254.7 Ma
-3.5
JS130-8
263.7 Ma
-4.8
JS130-10
-7.9
252.9 Ma
JS130-16
252.1 Ma
-1.4
JS133-4
252.2 Ma
-4.8
JS133-11
252.0 Ma
-3.3
JS133-14
-0.4
253.5 Ma
JS133-16
-5.5
252.1 Ma
JS135-1
252.6 Ma
-5.4
JS135-10
-8.0
252.4Ma
JS135-12
-6.2
251.6Ma
JS135-11
100μm
-2.1
270.8 Ma
JS129-6
273.7 Ma
JS133-12
U-Pb in CUG with 24 μm
Hf in CUG with 44 μm

B

Figure 3b


254.9 Ma
-2.5
MS25-2
252.5 Ma
-7.1
MS25-3
252.4 Ma
-6.3
MS25-4
252.4 Ma
-6.7
MS25-12
252.4 Ma
-6.9
MS25-14
-5.2
254.8 Ma
MS25-15
256.1 Ma
-6.7
MS26-6
-6.3
256.1 Ma
MS26-8
254.0 Ma
-5.2
MS26-14
-5.1
252.8 Ma
MS32-3
252.0 Ma
-5.0
MS32-11
-7.3
253.3 Ma
MS32-12
252.7 Ma
-6.5
MS32-15
-6.5
251.6 Ma
MS32-13
253.0 Ma
-7.5
MS37-12
254.1 Ma
-8.8
MS37-4
251.9Ma
-9.2
Ms37-7
250.9Ma
-6.8
Ms48-1
251.2 Ma
-7.6
MS48-3
254.9 Ma
-7.6
MS48-6
250.1 Ma
-9.0
MS48-9
253.3 Ma
-8.2
MS48-11
263.4 Ma
-8.3
MS48-13
251.3 Ma
-9.4
MS48-15
252.3 Ma
-8.4
MS48+1.3-5
253.7 Ma
-8.1
MS48+1.3-8
252.6 Ma
-7.0
MS48+1.3-10
252.6 Ma
-8.4
MS48+1.3-15
100μm
262.1 Ma
-8.0
MS37-1
270.0 Ma
-2.9
MS26-12
U-Pb in CUG with 24 μm
Hf in CUG with 44 μm

C

Figure 3c

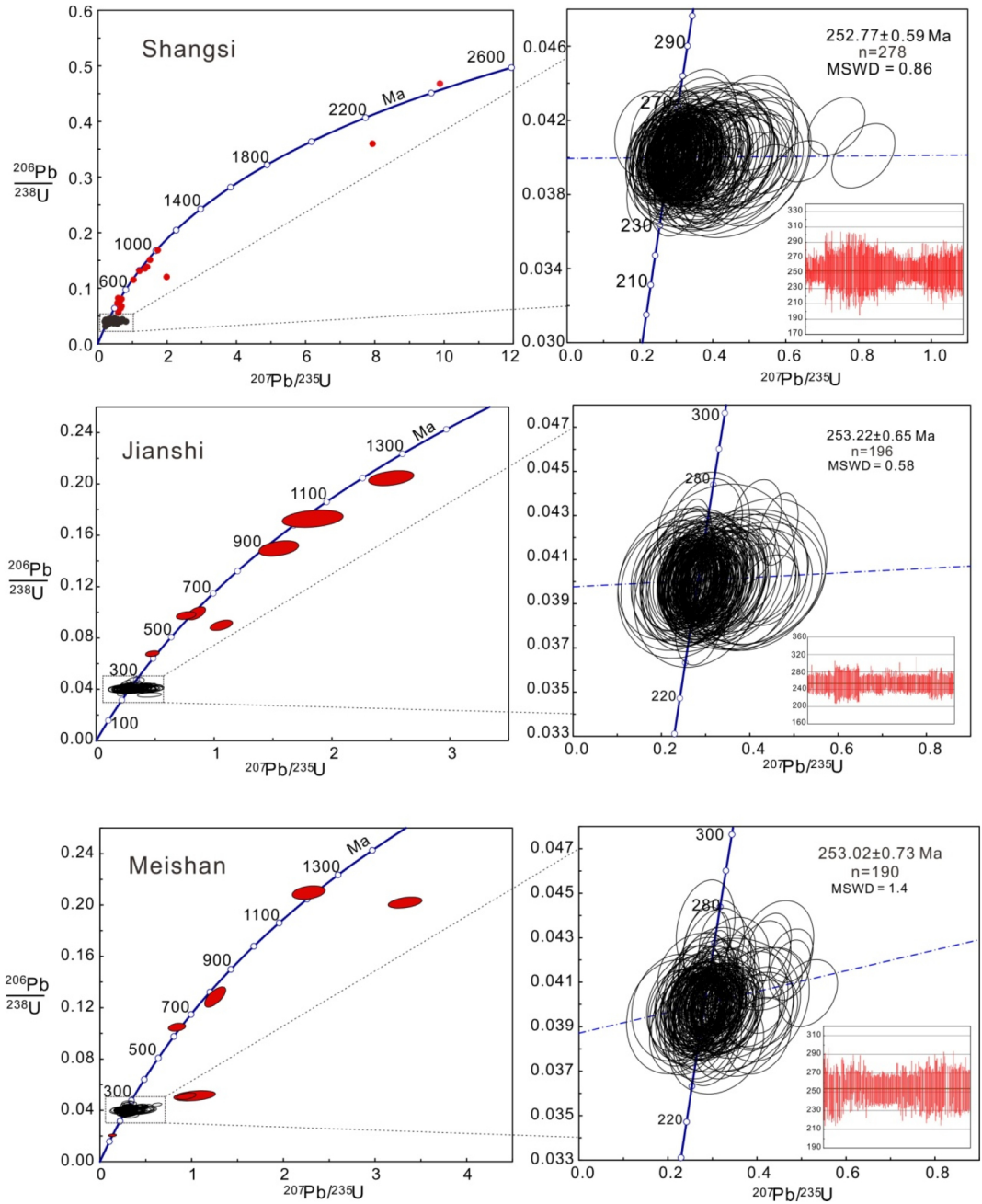
Shangsi
Ma
2600
2200
1800
1400
1000
600
$^{206}Pb/^{238}U$
$^{207}Pb/^{235}U$
252.77±0.59 Ma
n=278
MSWD = 0.86
290
270
230
210
Jianshi
1300
1100
900
700
500
300
100
253.22±0.65 Ma
n=196
MSWD = 0.58
280
220
Meishan
253.02±0.73 Ma
n=190
MSWD = 1.4

Figure 4

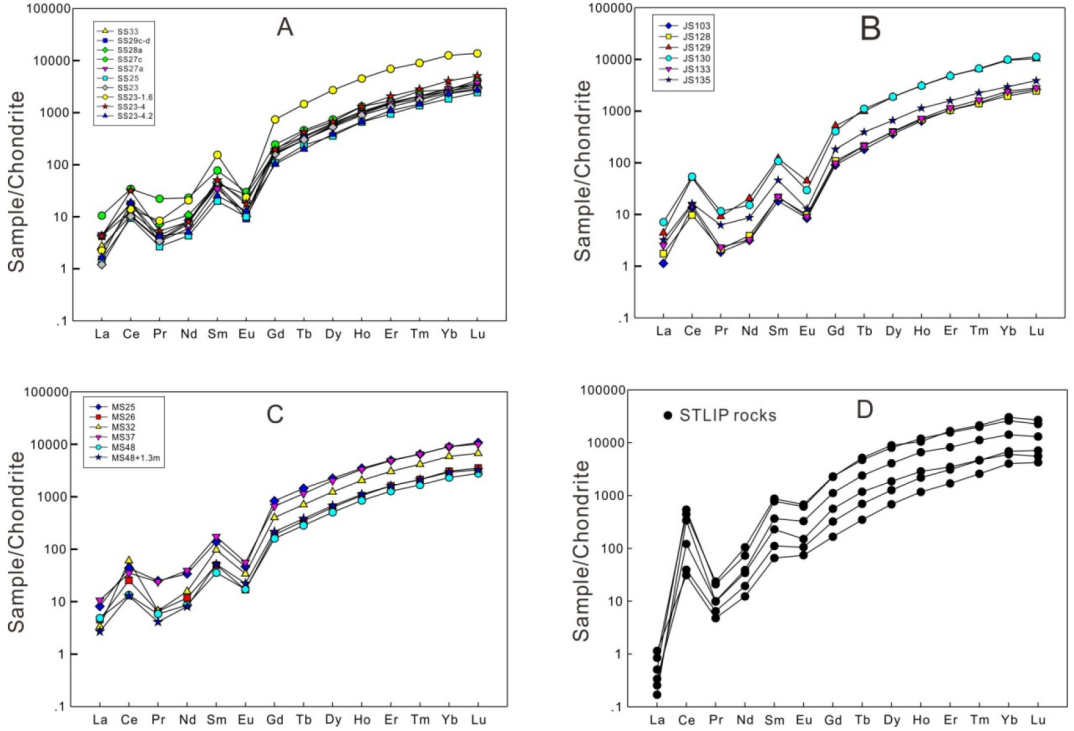
A
SS33
SS29c-d
SS28a
SS27c
SS27a
SS25
SS23
SS23-1.6
SS23-4
SS23-4.2
B
JS103
JS128
JS129
JS130
JS133
JS135
C
MS25
MS26
MS32
MS37
MS48
MS48+1.3m
D
STLIP rocks
Sample/Chondrite
100000
10000
1000
100
10
1
.1
La Ce Pr Nd Sm Eu Gd Tb Dy Ho Er Tm Yb Lu

Figure 5

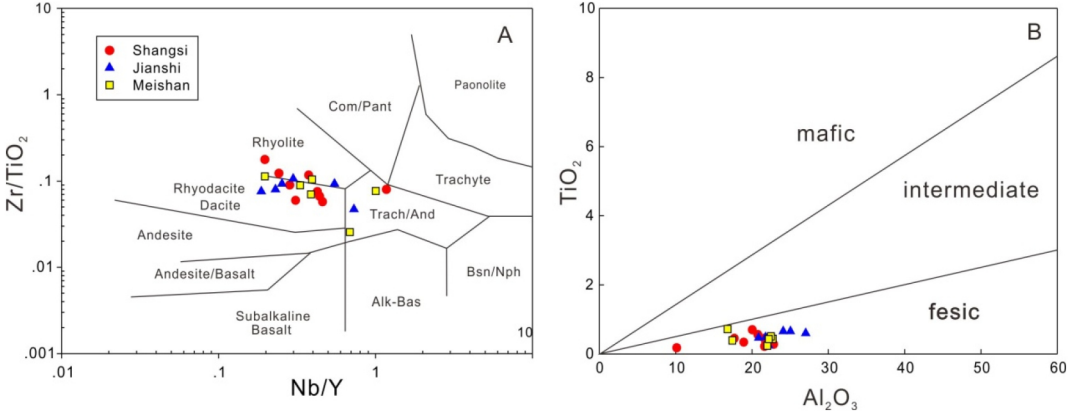
A
Shangsi
Jianshi
Meishan
Paonolite
Com/Pant
Rhyolite
Trachyte
Rhyodacite
Dacite
Trach/And
Andesite
Andesite/Basalt
Bsn/Nph
Alk-Bas
Subalkaline
Basalt
Zr/TiO2
Nb/Y
10
1
.1
.01
.001
B
mafic
intermediate
fesic
TiO2
Al2O3
0
2
4
6
8
10
20
30
40
50
60

Figure 6

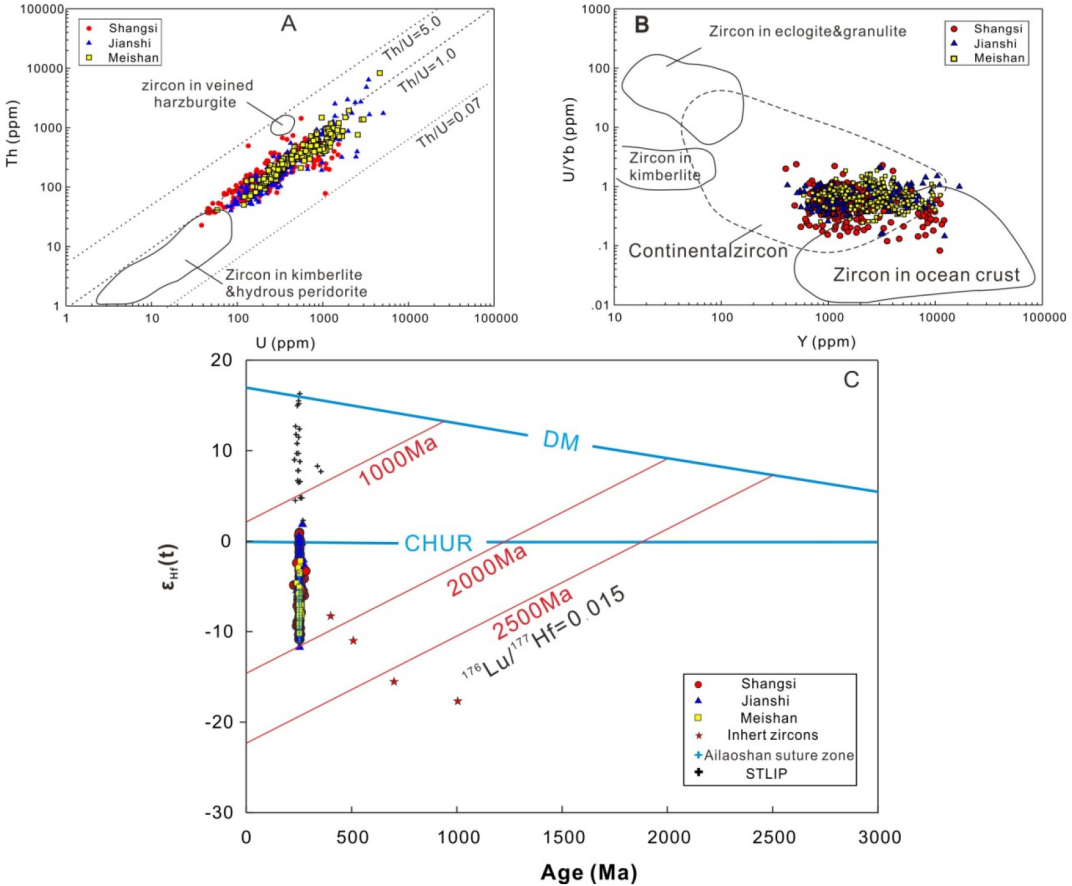
A
Shangsi
Jianshi
Meishan
Th/U=5.0
Th/U=1.0
Th/U=0.07
zircon in veined harzburgite
Zircon in kimberlite &hydrous peridorite
Th (ppm)
U (ppm)
B
Zircon in eclogite&granulite
Zircon in kimberlite
Continentalzircon
Zircon in ocean crust
U/Yb (ppm)
Y (ppm)
C
DM
1000Ma
CHUR
2000Ma
2500Ma
176Lu/177Hf=0.015
Inhert zircons
Ailaoshan suture zone
STLIP
εHf(t)
Age (Ma)

Figure 7

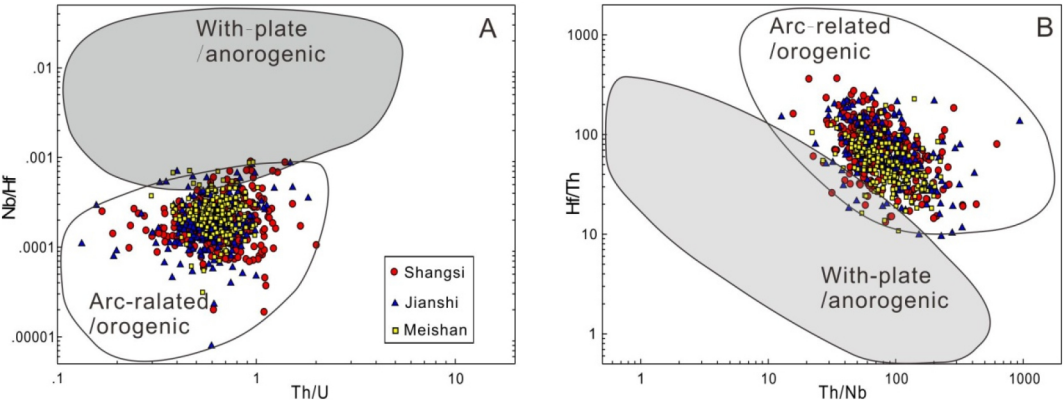
A
With-plate
/anorogenic
Arc-ralated
/orogenic
Nb/Hf
.01
.001
.0001
.00001
.1
1
10
Th/U
Shangsi
Jianshi
Meishan
B
Arc-related
/orogenic
With-plate
/anorogenic
Hf/Th
1000
100
10
1
1
10
100
1000
Th/Nb

Figure 8

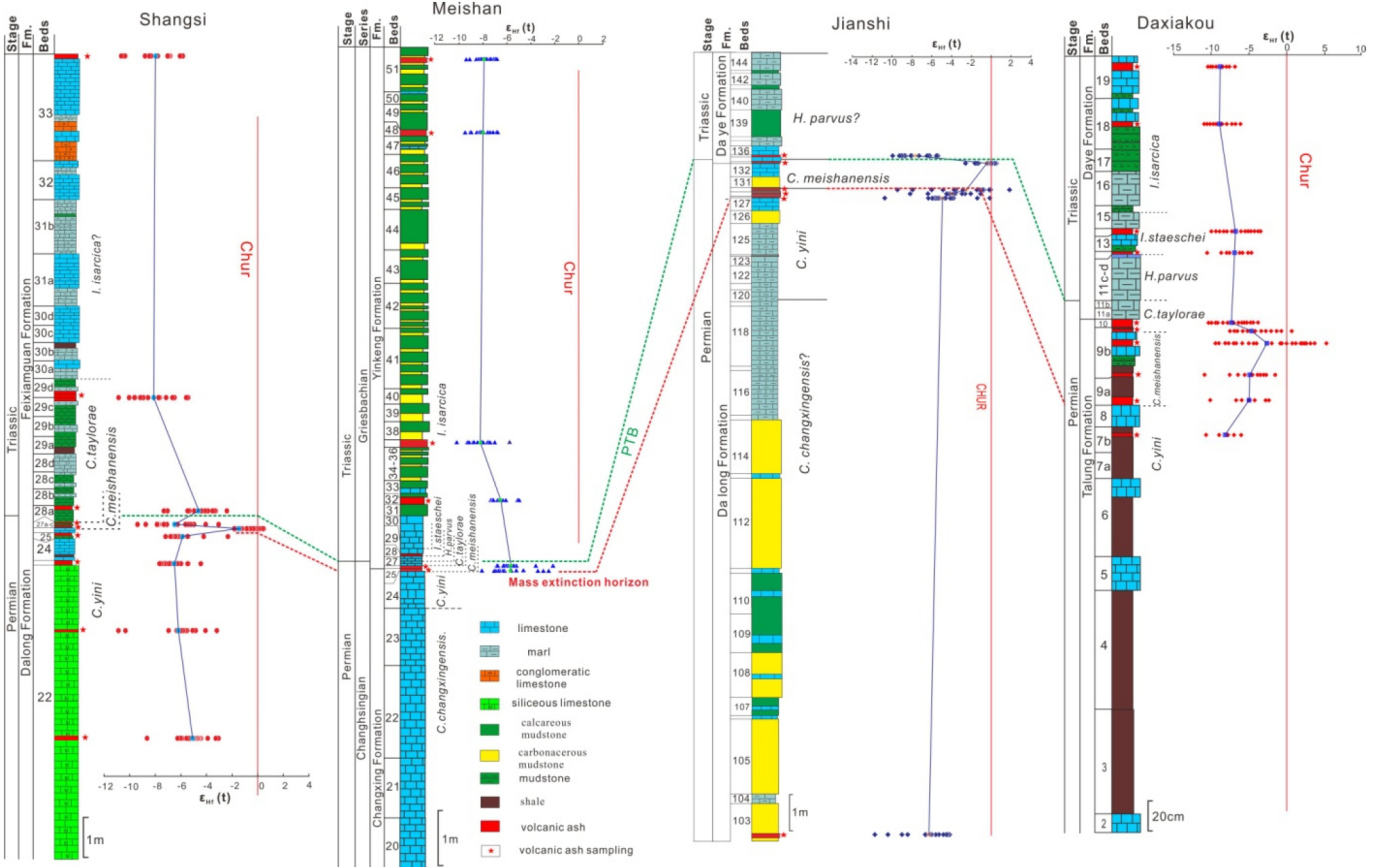
Shangsi
Meishan
Jianshi
Daxiakou
Stage
Fm.
Beds
Series
Triassic
Permian
Griesbachian
Changhsingian
Feixianguan Formation
Dalong Formation
Yinkeng Formation
Changxing Formation
Daye Formation
Talung Formation
Chur
CHUR
PTB
Mass extinction horizon
I. isarcica?
I. isarcica
I.staeschei
H.parvus
C.taylorae
C. meishanensis
C.yini
C. changxingensis?
C. changxingensis.
H. parvus?
1m
20cm
limestone
marl
conglomeratic limestone
siliceous limestone
calcareous mudstone
carbonaceous mudstone
mudstone
shale
volcanic ash
volcanic ash sampling

Figure 9